
Integrated Gradient Correlation: a Dataset-wise Attribution Method

Pierre Lelièvre^{*} ¹ Chien-Chung Chen¹

Abstract

Attribution methods are primarily designed to study input component contributions to individual model predictions. However, some research applications require a summary of attribution patterns across the entire dataset to facilitate the interpretability of the scrutinized models at a task-level rather than an instance-level. It specifically applies when the localization of important input information is supposed to be *stable* for a specific problem but remains unidentified among numerous components. In this paper, we present a dataset-wise attribution method called Integrated Gradient Correlation (IGC) that enables region-specific analysis by a direct summation over associated components, and further relates the sum of all attributions to a model prediction score (correlation). We demonstrate IGC on synthetic data and fMRI neural signals (NSD dataset) with the study of the representation of image features in the brain and the estimation of the visual receptive field of neural populations. The resulting IGC attributions reveal selective patterns, coherent with respective model objectives.

1. Motivation

Existing attribution methods study input component contributions to individual model predictions. Here, we investigate the problem of summarizing these attributions at a dataset level. We particularly search for a method fulfilling the interpretability requirements of modeling scenarios such as *Where a specific image feature is represented in the visual cortex of the human brain? What is the visual receptive field of a population of neurons?* (see Section.5 for details). These examples have in common to call for the exposition of which input components are responsible for achieving the overall task, and not specific entries. An

^{*}Git repository ¹Department of Psychology, National Taiwan University, Taipei, Taiwan. Correspondence to: Pierre Lelièvre <contact@plelievre.com>.

Preprint. Under review.

implicit condition of these scenarios is thus a relatively *stable* localization of important input information across the dataset, at least for each specific task. For instance, it works with functional Magnetic Resonance Imaging (fMRI), where each voxel/vertex represents an invariant brain area, covering a population of neurons. On the other hand, in the context of image content recognition, a *dataset-wise attribution method* would not be pertinent because a *cat* can appear anywhere in an image and still accurately trigger the *cat* class. While such a requirement can be perceived as a limitation, this is an intrinsic aspect of any dataset-wise inquiry (that do exist), and not of our resolving method.

Some research fields, such as neuroscience, heavily rely on linear models to straightforwardly associate prediction scores with input components. Modelers overcome inherent limitations with *linearized* data, based on handcrafted nonlinear data preprocessing. Although legitimate, such an approach is unlikely to produce perfect linear mappings. Only deep models could exploit nonlinear and multiscale interactions without *a priori* data domain adaptation. However, the lack of dataset-wise summary techniques leaves deep models with an interpretability issue.

Our method is therefore designed to be easily integrated in research activities and transparently used in place of linear regression analysis. To do so, it must fulfill requirements expressed in Naselaris et al. (2011) with the following questions: *Does an input region of interest (ROI), contain information about some specific set of output features? Are there specific ROIs that contain relatively more information about a specific set of features? Are there specific features that are preferentially represented by a single ROI?* We then identify three main specifications: **1)** a *dataset-wise attribution method* must permit a flexible definition of ROIs; **2)** relative ROI attributions must allow pertinent comparisons; **3)** dataset-wise attributions must enable comparisons between different features, and implicitly for identical features, but through different models.

1.1. General modeling context

We define deep models as a class of functions $f : \mathbb{R}^m \rightarrow \mathbb{R}$ by \mathcal{F} . These models predict a random variable $y \in \mathbb{R}$ from a random vector $\mathbf{x} \in \mathbb{R}^m$, and they are trained with n i.i.d

pairs of a dataset \mathcal{D} , so that $(\mathbf{x}, \mathbf{y}) \sim \mathcal{D} = \{(\mathbf{x}^{(i)}, y^{(i)})\}_{i=1}^n$.

2. Attribution methods for individual predictions

Available techniques for individual predictions arose from different research domains. For instance, the Shapley Value (Shapley, 1952) originated from the cooperative game theory. It addressed cost/gain sharing problems between players w.r.t their contributions to the outcome. Modern variants (Lundberg & Lee, 2017; Dhamdhere et al., 2020; Sundararajan & Najmi, 2020) reduced inherent computational cost, but it is still not suited for large input dimensionalities. More recently, image content recognition deep models prompted the development of methods displaying pixel arrangements responsible for a classification decision (Zeiler & Fergus, 2013). Being differentiable, these models led to techniques exploiting gradient back-propagation for a lower computational cost (Baehrens et al., 2009; Simonyan et al., 2014). However, naive gradients encounter issues with activation functions such as ReLU, as it back-propagates zero gradients for negative inputs. Consequently, methods like guided back-propagation (Springenberg et al., 2015), GradCAM (Selvaraju et al., 2016; Chattopadhyay et al., 2018), LRP (Binder et al., 2016), or DeepLift (Shrikumar et al., 2019) operated architectural tweaks to avoid attribution shortcomings. Other methods also include Zhou et al. (2015); Ribeiro et al. (2016); Zintgraf et al. (2017).

An alternative to prevent spurious gradients is to compare attributions of the input under scrutiny with a baseline. This way, even if some input components receive zero gradients, their comparison with possibly non-zero baseline gradients reveals more correct contributions. Among popular *baseline attribution methods*, we find *path methods* and particularly *Integrated Gradients* (IG) (Sundararajan et al., 2017). Based on Aumann & Shapley (1974), IG aggregates the gradients of linearly interpolated inputs, following the shortest line from the baseline to the input (with all component attributions updated at once for few forward/backward passes through the model). For instance, another *path method* like Baseline Shapley (BS) (Sundararajan & Najmi, 2020) requires successive activations of each input component, making it longer to compute than IG by several folds. Although popular, *path methods* still exhibit unresolved issues, such as the optimality of selected path (Kapishnikov et al., 2021; Sanyal & Ren, 2021; Kawai et al., 2022) or the choice of the most appropriate baseline (Smilkov et al., 2017; Fong & Vedaldi, 2017; Lundberg & Lee, 2017; Erion et al., 2020; Sturmfels et al., 2020; Xu et al., 2020; Pan et al., 2021; Tan, 2022; Liu et al., 2023).

Our definition of *dataset-wise attribution methods* is built upon existing methods for individual predictions. It particularly requires desirable properties (axioms) that are only

satisfied by *path methods* (see Section.3). We will therefore briefly detail this class of methods, while referring to Lundstrom et al. (2022) for an in-depth analysis.

2.1. Path methods

A function $\gamma : \mathbb{R}^m \times \mathbb{R}^m \times [0, 1] \rightarrow \mathbb{R}^m$ is a *path function* if for any fixed input $\mathbf{x}^{(i)}$ and baseline $\bar{\mathbf{x}}$, γ is a continuous and piece-wise smooth curve from $\bar{\mathbf{x}}$ to $\mathbf{x}^{(i)}$ over t . This class of functions is represented by \mathcal{G} , and intermediary inputs are defined as $\mathbf{x}^{(t)} = \gamma(\mathbf{x}^{(i)}, \bar{\mathbf{x}}, t)$.

Given functions f and γ , fixed input $\mathbf{x}^{(i)}$ and baseline $\bar{\mathbf{x}}$, a *path method* is a function of the form $a : \mathcal{F} \times \mathcal{G} \times \mathbb{R}^m \times \mathbb{R}^m \rightarrow \mathbb{R}^m$. The contribution of $\mathbf{x}^{(i)}$ components to the individual prediction $f(\mathbf{x}^{(i)})$ are denominated by the vector $\mathbf{a}^{(i)} = a(f, \gamma, \mathbf{x}^{(i)}, \bar{\mathbf{x}})$, which j -th component is given by:

$$\mathbf{a}_j^{(i)} = \int_0^1 \frac{\partial f}{\partial \mathbf{x}_j^{(t)}}(\gamma(\mathbf{x}^{(i)}, \bar{\mathbf{x}}, t)) \times \frac{\partial \gamma_j}{\partial t}(\mathbf{x}^{(i)}, \bar{\mathbf{x}}, t) dt \quad (1)$$

Function f is already supposed to be differentiable because deep models are trained *via* SGD-like algorithms. However, *path methods* further imply that partial derivatives $\partial f / \partial \mathbf{x}_j^{(t)}$ exist for all $\mathbf{x}^{(t)}$ *almost everywhere*.¹

The baseline $\bar{\mathbf{x}}$ is similar to $\mathbf{x}^{(i)}$ in terms of dimensionality, but it can be arbitrarily set to any value. Zeros can simulate the least informational input in many cases, e.g., a black image. Nonetheless, defining a relevant baseline is difficult in some scenarios. For instance, the activity of the brain in a resting state is rarely flat to zero. In such situations, we can turn the baseline into a random vector $\bar{\mathbf{x}}$ sampled from any distribution, and further consolidate attributions by taking their expected value (Lundberg & Lee, 2017; Erion et al., 2020). The choice of the baseline distribution is commonly the dataset \mathcal{D} itself, so that:

$$a_j(f, \gamma, \mathbf{x}^{(i)}, \bar{\mathbf{x}}) = \mathbb{E}_{\bar{\mathbf{x}} \sim \mathcal{D}} \left[a_j(f, \gamma, \mathbf{x}^{(i)}, \bar{\mathbf{x}}^{(k)}) \right] \quad (2)$$

Random baseline path methods fulfill a similar set of axioms as original *path methods*, and the following definitions could be easily adapted to this variant. We use it in practice, but we will keep the single baseline paradigm for legibility.

Dummy This first axiom intuitively means that an input component having no influence on model outputs should have zero attribution. In other word, if a partial derivative of f is zero for a component j , corresponding $\mathbf{a}_j^{(i)}$ is null.

Completeness In a cost/gain sharing context, *completeness* refers to the intuitive idea that the sum of all contributions must be equal to the cost/gain under scrutiny. More

¹It means that the points for which partial derivatives are not defined have Lebesgue measure 0.

generally, it means that the sum of all component attributions $\mathbf{a}_j^{(i)}$ must reflect the model prediction $f(\mathbf{x}^{(i)})$, so that:

$$\sum_{j=1}^m \mathbf{a}_j^{(i)} = f(\mathbf{x}^{(i)}) - f(\bar{\mathbf{x}}) \quad (3)$$

Implementation invariance Two functionally equivalent models (i.e. exhibiting comparable input/output behaviors), but with different architectures (e.g., the number of layers or the type of activation functions), should produce similar attributions. For instance, attribution methods that require low-level model modifications depending on selected activation functions, such as DeepLIFT (Shrikumar et al., 2019), break this axiom. In addition, the status of implied architectural changes becomes unclear when attempting to explain the default behavior of these models.²

3. Dataset-wise attribution methods

We define *dataset-wise attribution methods* as functions summarizing the distribution of component attributions for individual predictions $\mathbf{a}_j^{(i)}$ collected over the whole dataset \mathcal{D} and represented by the random vector \mathbf{a}_j . However, the isolated dynamic of \mathbf{a}_j , e.g., its mean or SD, is usually irrelevant (see Section.4 for illustrations). From the *completeness* axiom of *path methods*, we know that the overall magnitude of individual attributions is linearly modulated by the magnitude of model predictions $f(\mathbf{x})$. We therefore propose to summarize the distribution of \mathbf{a}_j by a measure of its linear relationship with predictions $f(\mathbf{x})$, i.e. a covariance-based analysis.

In addition, the third requirement described in Section.1 states that dataset-wise attributions must be comparable between models and thus implicitly reflect models' performance. The covariance between \mathbf{a}_j and *true* output y then appears an even more informative alternative. In the case of unavailable *true* output y , we still explore the first option mentioned above in Subsection.3.2. Finally, we introduce a scaling factor in our definition to enable interesting properties (see below).³

Given functions f and γ , random variables \mathbf{x} and y , and baseline $\bar{\mathbf{x}}$, a *dataset-wise attribution method* is a function of the form $b : \mathcal{F} \times \mathcal{G} \times \mathbb{R}^m \times \mathbb{R}^m \times \mathbb{R} \rightarrow \mathbb{R}^m$. Resulting attributions are denominated by the vector $\mathbf{b} = b(f, \gamma, \mathbf{x}, \bar{\mathbf{x}}, y)$, which j -th component is given by:

$$\mathbf{b}_j = \frac{1}{\sigma_{f(\mathbf{x})}\sigma_y} \mathbb{E}_{(\mathbf{x}, y) \sim \mathcal{D}} \left[\mathbf{a}_j^{(i)} \times (y^{(i)} - \mu_y) \right] \quad (4)$$

²*Path methods* also satisfy *linearity* (see Appendix.A.1), but this axiom is not necessary for the definition of our method.

³Despite the absence of apparent alternatives fulfilling the following properties, we leave the uniqueness of our proposition at a state of conjecture.

with $\sigma_{f(\mathbf{x})}$ and σ_y the standard deviations of $f(\mathbf{x})$ and y , and \mathbf{a}_j attributions given by a *path method* (see Eq.1).⁴

Dummy Similarly to *path methods*, our proposition is zero for an input component if the partial derivatives of f is zero for this component. In addition, *dummy* can be extended to input component for which attributions \mathbf{a}_j are independent of y , i.e. having zero covariance.

Implementation invariance This property is inherited from the supporting *path method*.⁵

Completeness to a model prediction score The first two interpretability requirements expressed in Section.1 impose that dataset-wise attributions can be easily aggregated. For any ROI \mathcal{R} , the summary $\mathbf{b}_{\mathcal{R}}$ is thus defined as a simple summation over input components.

$$\mathbf{b}_{\mathcal{R}} = \sum_{j \in \mathcal{R}} \mathbf{b}_j \quad (5)$$

Similarly to the *completeness* axiom of *path methods*, such an additive property is only meaningful if the total attribution over input components reflects an interesting characteristic of the model. Thanks to scaling $1/\sigma_{f(\mathbf{x})}\sigma_y$, our proposition sums to the correlation $\rho(f(\mathbf{x}), y)$ (see Appendix.A.2 for the proof). The total attribution is therefore related to a prediction score of the model, and fulfills the third requirement expressed in Section.1.

$$\sum_{j=1}^m \mathbf{b}_j = \rho(f(\mathbf{x}), y) \quad (6)$$

3.1. Supporting path method

Each *path method* provides different attributions since they take different paths from the baseline to the input. However, empirical results with two popular *path methods* (BS and IG) showed that BS does not produce significant differences from IG (see Appendix.A.4). Because of BS higher computational cost, we recommend IG in the general case. This is also the reason we coined our *dataset-wise attribution method*: Integrated Gradient Correlation (IGC).

By definition, IG is a *path method* with $\gamma^{\text{IG}}(\mathbf{x}^{(i)}, \bar{\mathbf{x}}, t) = \bar{\mathbf{x}} + t(\mathbf{x}^{(i)} - \bar{\mathbf{x}})$, i.e. a straight line between $\bar{\mathbf{x}}$ and $\mathbf{x}^{(i)}$. In practice, the integral of Eq.1 is replaced by its Riemman approximation with few discrete s steps (Sundararajan et al., 2017):

$$\mathbf{a}_j^{(i) \text{ IG}} \approx \frac{\mathbf{x}_j^{(i)} - \bar{\mathbf{x}}_j}{s} \sum_{t=1}^s \frac{\partial f}{\partial \mathbf{x}_j^{(t)}} \left(\bar{\mathbf{x}} + \frac{t}{s} (\mathbf{x}^{(i)} - \bar{\mathbf{x}}) \right) \quad (7)$$

⁴We omit the subtraction of $\mathbf{a}_j^{(i)}$ by the expected value of \mathbf{a}_j for legibility and the simplification of the *completeness* proof.

⁵We empirically demonstrate the relative independence of our method upon model implementations in Appendix.A.4.

3.2. Auto-correlation variant

IGC is primarily designed to explain a model and its associated dataset, but *true* outputs y may not be available when applied on new data. In this case, we propose an *auto-correlation* variant \mathbf{b}^* (IGaC), where y is replaced by $f(\mathbf{x})$ in Eq.4, so that:

$$\mathbf{b}_j^* = \frac{1}{\sigma_{f(\mathbf{x})}^2} \mathbb{E}_{\mathbf{x} \sim \mathcal{D}} \left[\mathbf{a}_j^{(i)} \times (f(\mathbf{x}^{(i)}) - \mu_{f(\mathbf{x})}) \right] \quad (8)$$

IGC properties are conserved except for *completeness* that sums to 1 instead of a model prediction score.

$$\sum_{j=1}^m \mathbf{b}_j^* = \rho(f(\mathbf{x}), f(\mathbf{x})) = 1 \quad (9)$$

3.3. IGC with categorical distributions

Our method is mainly elaborated for models predicting scalars. However, some modeling scenarios involve the prediction of random variables ruled by categorical distributions with K categories. Usually expressed as *one-hot* vectors, models predict probabilities p_k with $k \in [1, K]$. A prediction score based on the correlation between p_k and corresponding *true one-hot* vector components is not ideal, but effective (see Exp.D in Section.4). In addition, this setup allows the computation of dataset-wise attributions w.r.t. each class independently.

3.4. Practical IGC computation

To be dataset-wise relevant, IGC attributions require a representative (large enough) validation set. Conversely, the computation time of our method linearly scales up with the size of this set, and smaller sub-sets may be necessary in some contexts (e.g., extremely large datasets, limited computational resources). Under those circumstances, we advise checking if the absolute difference between the total sum of IGC attributions (computed on a subset) and the model correlation score (computed on the complete validation set) remains below an acceptable value. We used $1e-2$ in our experiments.

Nonetheless, reaching this figure necessitates relevant IG entries, computed with a number of steps (and random baselines) appropriate to the model complexity. Based on *completeness* (see Eq.3), we advise checking whether the mean absolute difference between the sum of IG components and its corresponding input/baseline difference is reasonable ($< 1e-3$ in our studies).

4. Benchmark

To our knowledge, there is no existing *dataset-wise attribution method* for comparison with IGC. The only available

baselines are naive aggregations of IG attributions, i.e. the mean and SD of their per-component distributions over the dataset.⁶ In addition, available quantitative methods to evaluate attribution methods for individual prediction like LeRF&MoRF (Samek et al., 2015) or ROAR (Hooker et al., 2019) are designed for classification endeavors. They require an ordering of input components from least to most relevant. It works for categorical tasks because an input component with a negative attribution indicates that it lowers the output probability of this class and thus increases the model uncertainty. On the contrary, for models predicting scalars, a negative attribution is not necessarily the least relevant, e.g., when the output is also negative.

In the current work, we therefore assess the relevancy of IGC attributions on synthetic experiments designed to reveal shortcomings of other propositions. We first define localized image statistics, e.g., the sum of pixel values weighted by a 2-d map, and then try to recover the generating masks/rules from the pairs of input image/output statistic. Images are randomly generated, but we enforce a spatial frequency distribution similar to natural images to guarantee a certain level of spatial redundancy (see Fig.A5 image examples and Appendix.A.3 for implementation details). To prevent implementation and training variabilities of deep models, presented attributions are computed through the *original* differentiable functions producing the statistics. Only *IGC (model)* attributions involve trained models for verification.⁷ The definition of the four experiments labeled Exp.A-D are detailed below and illustrated in Fig.1 (top/left row).

Experiment.A This is the sum of pixel values weighted by the difference of two centered Gaussians with opposite polarities. From Fig.1, it is clear that the mean of IG attributions is not suitable. It only produces residual noise.⁸ Indeed, as output values are standardized (as it is usually done to train deep models), *IG (mean)* attributions tend to be zero by *completeness*. For instance, if we consider a trivial and perfect model f predicting a standardized random scalar x from the same input x (i.e. learning identity), the IG value for any $x^{(i)}$ would be $x^{(i)}$, and *IG (mean)* attributions would be $\mathbb{E}_{\mathbf{x} \sim \mathcal{D}}[x^{(i)}] = 0$. Outcomes from *IG (SD)* look more appropriate. However, this alternative makes is incapable of negative attributions by definition. *IG (SD)* is thus missing important information that could lead to model strategy mis-

⁶In Appendix.A.4, we also report basic metrics not involving any model, such as per-component correlations and t-tests.

⁷R2 scores of the models dedicated to Exp.A,B,C are > 0.99 , > 0.99 , and 0.81 . For Exp.D, the Top-1 accuracy is 0.81 . Statistics for Exp.C,D involve some randomness naturally limiting maximum prediction scores. Appendix.A.5 reports architectural/training characteristics of implemented models and IGC computation details.

⁸Regions outside masks are perfectly zero because we use of gradients from original functions to compute the different attribution propositions. However, this is of little concern as observed shortcomings happen inside the masks.

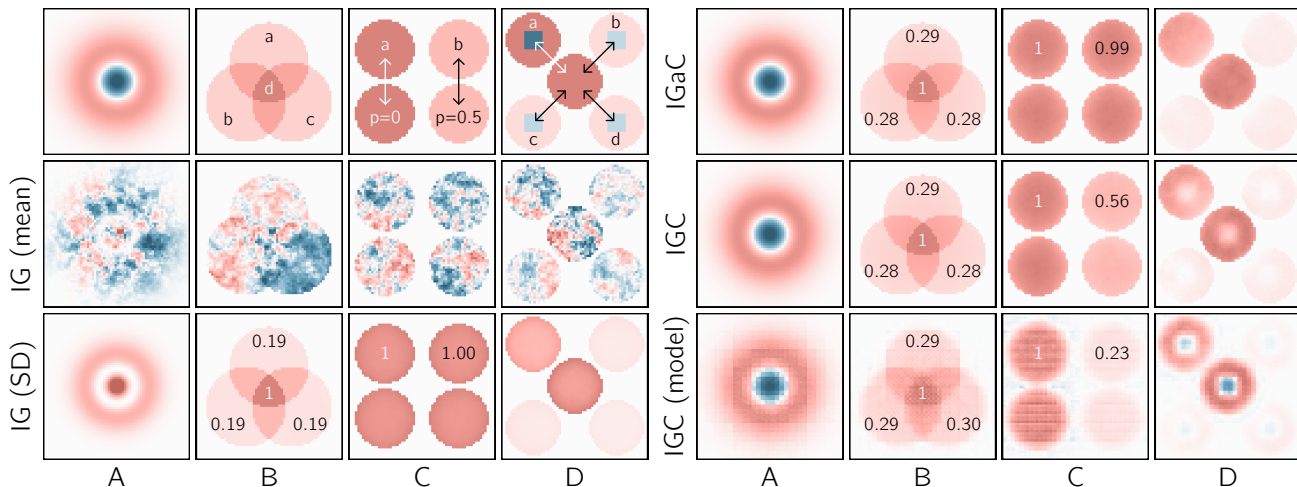


Figure 1. Benchmark of different propositions of *dataset-wise attribution methods* on four experiments labeled A-D. Attribution maps are individually scaled for a better visualization. Blue/red pixels indicate negative/positive values. See the main text for details about the experiments and for a discussion of displayed propositions.

interpretations. Only IGC, IGaC, and *IGC (model)* capture the expected attribution pattern.

Experiment.B We first compute the mean value of three independent circular regions, and then report the maximum value. The expected dataset-wise attribution is then the probability of each pixel to contribute to the output. As circles are partially overlapped, probabilities must sum at intersections. Once again, only IGC, IGaC, and *IGC (model)* capture the right balance of each area. For instance, the sum of individual densities (a, b, c) represent 85% of the central area (d) for IGC, where it is only 57% for *IG (SD)*.

Experiment.C The goal of Exp.C is to demonstrate the benefic of IGC over IGaC when there are large discrepancies between models predictions and *true* outputs. To simulate this phenomenon, we introduced some randomness during the computation of the statistic, so that when we calculate the attributions displayed in Fig.1, this initial random process is inaccessible. The statistic itself is computed in two steps. We first record the cosine similarity between two vertical pairs of circular regions (a, b), and then report the maximum value. The randomness is introduced in (b), having a probability $p = 0.5$ to be set to zero. Taking (a) as a reference, the mean attribution of (b) is similar to (a) for IGaC and about 0.56 for IGC. So, only IGC manages to reflect the uncertainty associated with (b). For *IGC (model)*, the model seems to further adapt to the reliability of the inputs, and (b) even drops to 0.23.

Experiment.D With Exp.D, we finally explore categorical outputs. We report the argmax of the cosine similarity

between a central circular area and four corner circles. Only, the first category (a) is reported (other classes being symmetrical). In addition, small squares in each corner circle are randomly substituted. Similarly to Exp.C, only IGC reveals unreliable areas (the corner square and the associated pixels in the central circle), for which IGaC is completely blind. With *IGC (model)*, these *spurious* squares are even assigned negative values. Indeed, a component that increases the model uncertainty about a category by lowering corresponding probability deserves a negative attribution.

Overall, IGC proved to be a non-trivial method, able to reveal important patterns that other propositions fail to exhibit. In addition, IGC fulfills *completeness to a model prediction score* that was not covered by this benchmark.

5. Applications

Integrated Gradient Correlation is applicable to a diversity of real modeling scenarios. Here, we present a decoding model of fMRI data that investigates the representation of image statistics in the brain, and an encoding model that estimates the visual receptive field of neural populations.⁹

5.1. Representation of image statistics in the brain

In neuroscience, fMRI is a widely used technique to measure the brain activity. Neural activations are captured through the proxy of the blood oxygenation level. This intermediary is relatively delayed from the underlying electric neural activity but provides high-resolution maps.

⁹Appendix.A.6 reports architectural/training characteristics of implemented models and IGC computation details.

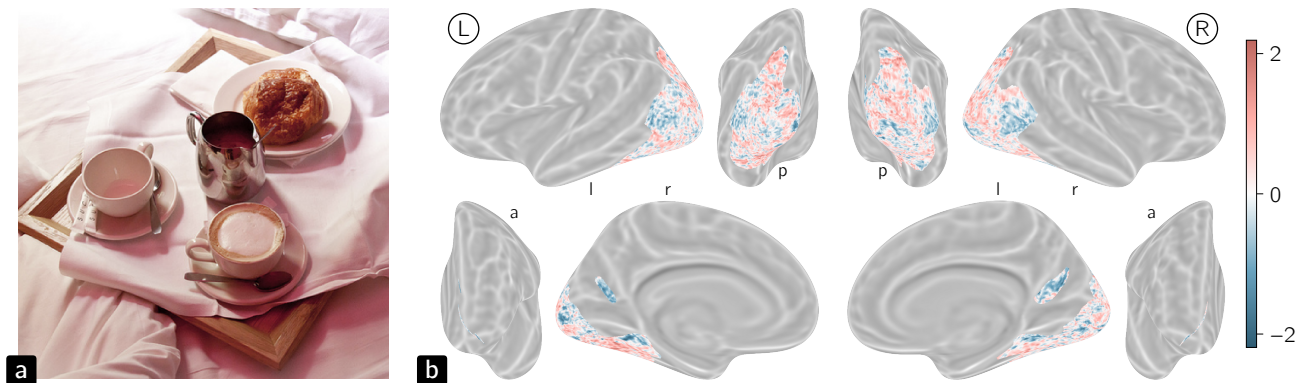


Figure 2. NSD dataset overview. Panel **a** displays an image as seen by the subject 1, and panel **b** shows corresponding fMRI activation maps for the left (L) and right (R) brain hemispheres. These surface-based fMRI data are projections from volumetric acquisitions to an average brain space and limited to the visual cortex. Per vertex activations over the dataset are standardized per subjects. For each hemisphere, letters a, l, r, and p denote anterior, left, right, and posterior views.

The recent publicly available *Natural Scenes Dataset* (NSD) (Allen et al., 2022) has been designed to enable machine learning inquiries on human vision. It offers fMRI data for >70k distinct images, acquired during a long-term recognition task with 8 subjects over one year. Selected images come from the COCO dataset (Lin et al., 2015) (see Fig.2a). The fMRI data are initially volume-based, with brain hemispheres discretized as voxels, but they can also be projected on the surface of the brain gray matter, which is a convoluted layer where most activations happen. As result, such a surface is easier to map to an average brain morphology shared by all participants (i.e. the *fsaverage* template of *FreeSurfer* software), and enables inter-subject data aggregation. Here, we focus on the visual cortex, i.e. two graphs of nearly 20k vertices each (see posterior areas of left and right hemispheres in Fig.2b).

For this first example, we build a model predicting two image statistics from fMRI data. We chose the luminance contrast (i.e. the SD of pixel luminance values) which is perhaps the most studied image variable in vision science. The second is *1/f slope*, a value related to spatial frequencies and relevant to our visual perception (Field, 1987; Tolhurst et al., 1992; Torralba & Oliva, 2003). The slope refers to the decreasing linear correspondence between log-intensities and spatial log-frequencies of natural images. Both features are computed globally on gray-scaled images. Our model is a simple multilayer perceptron (6 layers) with batch-normalization (Ioffe & Szegedy, 2015) and Mish activation functions (Misra, 2020). Despite the morphological mapping to an average brain, the functional behavior of each vertex may differ from one subject to another. As a result, the first layer is optimized per subject and serves as an adaptation interface. The average R2 score is 0.39.

Fig.3a,b show resulting IGC attributions for the first subject. In overlay, we display V1 to V4 ROIs that constitute the beginning of the visual pathway in the brain. Early convolutional blocks of image content recognition deep models, such as AlexNet (Krizhevsky et al., 2012) or VGG (Simonyan & Zisserman, 2014) share some arguable degrees of similarity with these early visual ROIs (Yamins & DiCarlo, 2016; Eickenberg et al., 2017; Neri, 2022). For the luminance contrast in Fig.3a, we observe that V1 contributions are strongly positive (in red), while V2 and V3 attributions appear negative (in blue). On the other hand, Fig.3b displays a more diffuse activation pattern for *1/f slope*, especially occurring beyond V1 to V4.

Due to the additive property of IGC attributions (see Eq.5), a more quantitative analysis is possible by a direct summation over ROIs. Fig.3c then consolidates previously observed trends for all subjects. Nonetheless, how to interpret negative attributions found in V2 for the luminance contrast? Contrary to categorical models, where inputs that systematically negatively contribute to the predictions can be interpreted as increasing the uncertainty of the model, negative IGC values found in models predicting scalars should rather be understood as an adjusting mechanism, balancing an overestimation resulting from positive regions. Therefore, V2 probably serves as a counterbalance to V1, which provides most of the global image luminance contrast estimation. The literature indicates that neurons with large receptive fields and associated with the peripheral vision are already present in V1, so that the strategy revealed by our method seems plausible to reflect real neural mechanisms. Another aspect making us confident about IGC findings, is that higher-level brain areas dedicated to large objects like *bodies* and *places* appear more relevant to the task than ROIs assigned to smaller content such as *words* and *faces*.

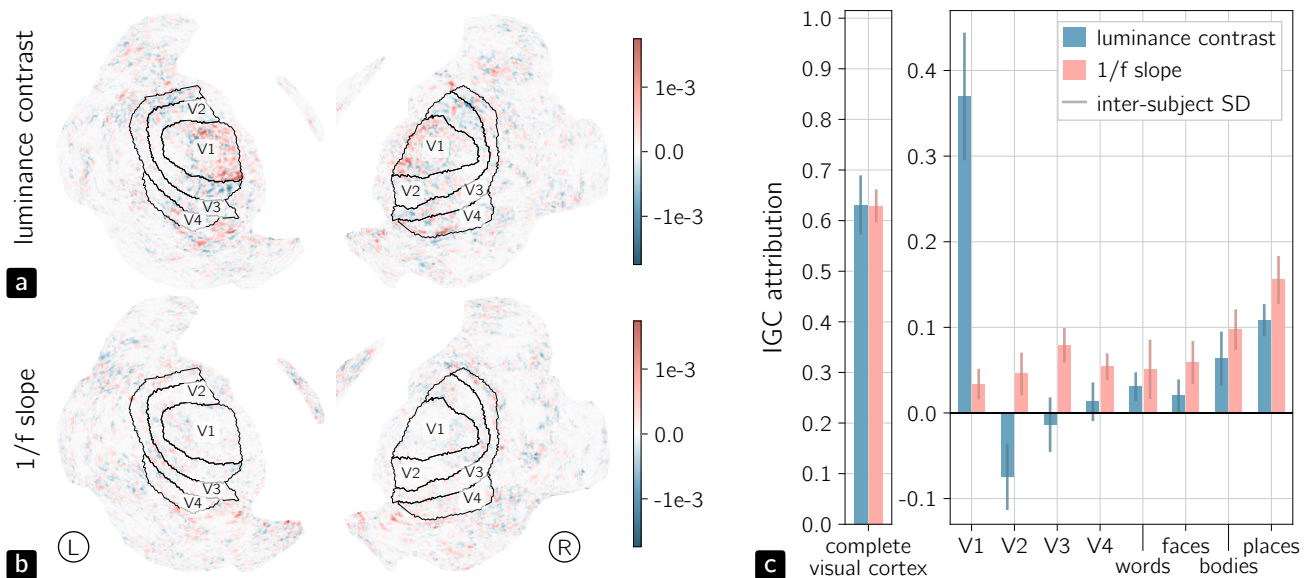


Figure 3. IGC attributions associated with the prediction of image statistics from fMRI data: luminance contrast (panel a) and $1/f$ slope (panel b). IGC maps and outlines of early visual ROIs (V1 to V4) correspond to the subject 1 of the NSD dataset. Higher level ROIs (e.g., *bodies* or *faces*) are not represented for legibility because of their scattered nature. Panel c displays an ROI-based summary of IGC attributions. Error bars reflect inter-subject variability (1 SD).

Concerning $1/f$ slope, IGC demonstrates a contrasting attribution distribution over the visual pathway. Fig.3c presents a more even use of all areas, with a preference for higher-level ROIs. This distinct strategy is in fact pertinent for a statistic summarizing spatial frequencies because the hierarchical processing of multiscale information is an inherent characteristic of our complete visual system.

5.2. Visual receptive field of neural populations

Neurons in early visual areas have been proved to be spatially specialized (Engel, 1997; Tyler et al., 2005; Wandell et al., 2005; 2007; Mackey et al., 2017; Benson et al., 2018). The population receptive field (pRF) then refers to the localized image area for which a group of neurons is responsive. Hierarchically folded repetitions of the visual field in the brain are even what enable the definition of V1 to V4 ROIs. With a long history in neuroscience, this functional identification of brain regions has been addressed with protocols involving artificial stimuli and a brute-force estimation of model parameters. Instead, we aim at providing pRF data with a wider and more ecological validity than the traditional approach by using our method on a deep encoding model predicting brain signals from natural images.

Specifically, we use the fMRI data of the NSD dataset restricted to the union of all subjects' V1, and associated images downsampled to 64 pixels. Our model consists of a ConvNeXt convolutional architecture (1 stem + 4 blocks)

(Liu et al., 2022), followed by two fully connected layers using batch-normalization and Mish activation functions. Because of subjects' residual morphological differences (see previous experiment for details), the last linear layer is optimized per subject and serves as an adaptation interface. The average R2 score is 0.36 (see Fig.4e).

For a selection of 6 vertices located in V1 of the subject 1 of the NSD dataset, Fig.4a shows that resulting IGC attributions give a direct visualization of the pRF associated with each vertex. pRF are traditionally modeled by 2-dimensional Gaussian distributions with a center (mean) expressed in polar coordinates, i.e. angle and eccentricity (see information overlaid on vertex b). From IGC maps, the fitting procedure is straightforward, and estimated pRF are represented by circles of radius 1 SD. Fig.4b,c,d display fitted parameters of all V1 vertices. Eccentricity and size are expressed in degrees of visual angle. The image size is 8.4° . Overall results are smooth and correspond to our expectations from the literature. Angles depicted in Fig.4b reflect the spatial inversion of images on our retina, e.g., the right side of images is represented in the left hemisphere. In addition, eccentricity and size (Fig.4c,d) exhibit some correlation. pRF are smaller at the center of images corresponding to our fovea. Nonetheless, there are some *spurious* regions, like around vertex f (see Fig.4b). From the IGC map (Fig.4a), we understand that this is due to a bi-modal receptive field that a 2-dimensional Gaussian cannot handle by definition. These anomalies are therefore due to the data

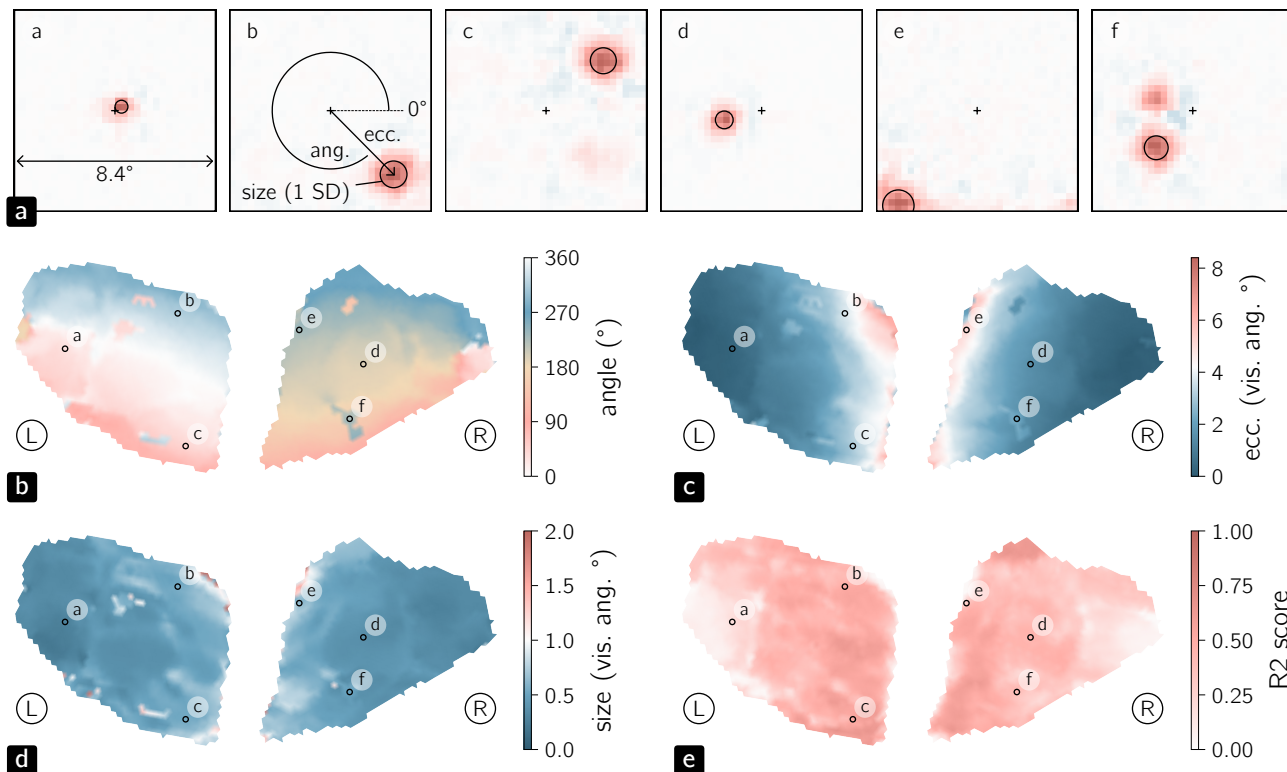


Figure 4. pRF estimation from IGC attributions associated with the prediction of the brain activity (fMRI data) from corresponding image stimuli. Panel a shows a selection of vertices located in V1 of the subject 1 of the NSD dataset. Circles indicate fitted pRF (1 SD) and central small crosses the fixation point of the participants. Panels b,c,d display pRF parameters (angle, eccentricity, and size) for all vertices of V1. The encoding accuracy R2 of our model is presented in panel e. Vertex labels a-f correspond between panels.

preprocessing rather than an inaccuracy of our method.

6. Conclusion

In this paper, we introduced the concept of *dataset-wise attribution methods* as functions summarizing the distribution of component attributions obtained with existing *path methods* for individual predictions. Our definition is axiomatic with the following desirable characteristics: 1) ROI attributions are computed as the sum of associated components; 2) the total attribution matches a prediction score of the model under inspection. In particular, we use *correlation* as a versatile prediction score and Integrated Gradients as a supporting *path method*. Integrated Gradient Correlation therefore inherits from IG an easy implementation and an applicability to high-dimensional datasets or highly non-linear models, as long as studied models are differentiable and that the number of IG steps is appropriate for the model complexity.

Furthermore, IGC attributions are designed to be *task-relevant* rather than *instance-relevant*. One typical use is when multiple features can be predicted from the same pool

of data, and that the respective localization of important input information is still unidentified among numerous components. Such a modeling scheme then naturally meets the only requirement to obtain meaningful IGC attributions, i.e. a *stable* localization of input information for each task under scrutiny.

Finally, through synthetic and practical applications, we demonstrated that IGC attributions reveal selective patterns, coherent with respective model objectives.

Acknowledgements

Supported by the National Science and Technology Council (NSTC). Collection of the NSD dataset was supported by NSF IIS-1822683 and NSF IIS-1822929.

Impact Statement

Our method is primarily designed to improve deep models interpretability, and it does not provide direct generative abilities, nor misuses we can identify. As result, we did not address further societal impact in the paper.

References

- Allen, E. J., St-Yves, G., Wu, Y., Breedlove, J. L., Prince, J. S., Dowdle, L. T., Nau, M., Caron, B., Pestilli, F., Charest, I., Hutchinson, J. B., Naselaris, T., and Kay, K. A massive 7T fMRI dataset to bridge cognitive neuroscience and artificial intelligence. *Nature Neuroscience*, 25(1): 116–126, January 2022. ISSN 1097-6256, 1546-1726. doi:10.1038/s41593-021-00962-x.
- Aumann, R. J. and Shapley, L. S. *Values of Non-Atomic Games*. Princeton University Press, Princeton, N.J, 1974. ISBN 978-0-691-08103-8.
- Baehrens, D., Schroeter, T., Harmeling, S., Kawanabe, M., Hansen, K., and Mueller, K.-R. How to Explain Individual Classification Decisions, December 2009. doi:10.48550/arXiv.0912.1128.
- Benson, N. C., Jamison, K. W., Arcaro, M. J., Vu, A. T., Glasser, M. F., Coalson, T. S., Van Essen, D. C., Yacoub, E., Ugurbil, K., Winawer, J., and Kay, K. The Human Connectome Project 7 Tesla retinotopy dataset: Description and population receptive field analysis. *Journal of Vision*, 18(13):23, December 2018. ISSN 1534-7362. doi:10.1167/18.13.23.
- Binder, A., Montavon, G., Bach, S., Müller, K.-R., and Samek, W. Layer-wise Relevance Propagation for Neural Networks with Local Renormalization Layers, April 2016. URL <http://arxiv.org/abs/1604.00825>.
- Chattopadhyay, A., Sarkar, A., Howlader, P., and Balasubramanian, V. N. Grad-CAM++: Improved Visual Explanations for Deep Convolutional Networks. In *2018 IEEE Winter Conference on Applications of Computer Vision (WACV)*, pp. 839–847, March 2018. doi:10.1109/WACV.2018.00097.
- Dhamdhere, K., Agarwal, A., and Sundararajan, M. The Shapley Taylor Interaction Index, February 2020. URL <http://arxiv.org/abs/1902.05622>.
- Eickenberg, M., Gramfort, A., Varoquaux, G., and Thirion, B. Seeing it all: Convolutional network layers map the function of the human visual system. *NeuroImage*, 152:184–194, May 2017. ISSN 10538119. doi:10.1016/j.neuroimage.2016.10.001.
- Engel, S. Retinotopic organization in human visual cortex and the spatial precision of functional MRI. *Cerebral Cortex*, 7(2):181–192, March 1997. ISSN 14602199. doi:10.1093/cercor/7.2.181.
- Erion, G., Janizek, J. D., Sturmfels, P., Lundberg, S., and Lee, S.-I. Improving performance of deep learning models with axiomatic attribution priors and expected gradients, November 2020. URL <http://arxiv.org/abs/1906.10670>.
- Field, D. J. Relations between the statistics of natural images and the response properties of cortical cells. *Journal of the Optical Society of America A*, 4(12): 2379, December 1987. ISSN 1084-7529, 1520-8532. doi:10.1364/JOSAA.4.002379.
- Fong, R. and Vedaldi, A. Interpretable Explanations of Black Boxes by Meaningful Perturbation. In *2017 IEEE International Conference on Computer Vision (ICCV)*, pp. 3449–3457, October 2017. doi:10.1109/ICCV.2017.371.
- Glorot, X. and Bengio, Y. Understanding the difficulty of training deep feedforward neural networks. In Teh, Y. W. and Titterton, M. (eds.), *Proceedings of the Thirteenth International Conference on Artificial Intelligence and Statistics*, volume 9 of *Proceedings of Machine Learning Research*, pp. 249–256, Chia Laguna Resort, Sardinia, Italy, May 2010. PMLR. URL <https://proceedings.mlr.press/v9/glorot10a.html>.
- He, K., Zhang, X., Ren, S., and Sun, J. Delving Deep into Rectifiers: Surpassing Human-Level Performance on ImageNet Classification. *arXiv:1502.01852 [cs]*, February 2015. URL <http://arxiv.org/abs/1502.01852>.
- Hooker, S., Erhan, D., Kindermans, P.-J., and Kim, B. A Benchmark for Interpretability Methods in Deep Neural Networks, November 2019. URL <http://arxiv.org/abs/1806.10758>.
- Ioffe, S. and Szegedy, C. Batch Normalization: Accelerating Deep Network Training by Reducing Internal Covariate Shift, March 2015. URL <http://arxiv.org/abs/1502.03167>.
- Kapishnikov, A., Venugopalan, S., Avci, B., Wedin, B., Terry, M., and Bolukbasi, T. Guided Integrated Gradients: An Adaptive Path Method for Removing Noise, June 2021. URL <http://arxiv.org/abs/2106.09788>.
- Kawai, Y., Tachikawa, K., Park, J., and Asada, M. Compensated Integrated Gradients for Reliable Explanation of Electroencephalogram Signal Classification. *Brain Sciences*, 12(7):849, June 2022. ISSN 2076-3425. doi:10.3390/brainsci12070849.
- Kingma, D. P. and Ba, J. Adam: A Method for Stochastic Optimization. *arXiv:1412.6980 [cs]*, January 2017. URL <http://arxiv.org/abs/1412.6980>.
- Krizhevsky, A., Sutskever, I., and E. Hinton, G. ImageNet Classification with Deep Convolutional Neural Networks. *Neural Information Processing Systems*, 25, January 2012. doi:10.1145/3065386.

- Lelièvre, P. Integrated Gradient Correlation. Zenodo, July 2025. doi:10.5281/ZENODO.15852412.
- Lin, T.-Y., Maire, M., Belongie, S., Bourdev, L., Girshick, R., Hays, J., Perona, P., Ramanan, D., Zitnick, C. L., and Dollár, P. Microsoft COCO: Common Objects in Context, February 2015. URL <http://arxiv.org/abs/1405.0312>.
- Liu, S., Chen, Z., Shi, G., Wang, J., Fan, C., Xiong, Y., Hu, R. W. Y., Ji, Z., and Gao, Y. Rethink Baseline of Integrated Gradients from the Perspective of Shapley Value, October 2023. URL <http://arxiv.org/abs/2310.04821>.
- Liu, Z., Mao, H., Wu, C.-Y., Feichtenhofer, C., Darrell, T., and Xie, S. A ConvNet for the 2020s, March 2022. URL <http://arxiv.org/abs/2201.03545>.
- Lundberg, S. and Lee, S.-I. A Unified Approach to Interpreting Model Predictions, November 2017. URL <http://arxiv.org/abs/1705.07874>.
- Lundstrom, D., Huang, T., and Razaviyayn, M. A Rigorous Study of Integrated Gradients Method and Extensions to Internal Neuron Attributions, June 2022. URL <http://arxiv.org/abs/2202.11912>.
- Mackey, W. E., Winawer, J., and Curtis, C. E. Visual field map clusters in human frontoparietal cortex. *eLife*, 6:e22974, June 2017. ISSN 2050-084X. doi:10.7554/eLife.22974.
- Misra, D. Mish: A Self Regularized Non-Monotonic Activation Function, August 2020. URL <http://arxiv.org/abs/1908.08681>.
- Naselaris, T., Kay, K. N., Nishimoto, S., and Gallant, J. L. Encoding and decoding in fMRI. *NeuroImage*, 56(2):400–410, May 2011. ISSN 10538119. doi:10.1016/j.neuroimage.2010.07.073.
- Neri, P. Deep networks may capture biological behavior for shallow, but not deep, empirical characterizations. *Neural Networks*, 152:244–266, August 2022. ISSN 08936080. doi:10.1016/j.neunet.2022.04.023.
- Pan, D., Li, X., and Zhu, D. Explaining Deep Neural Network Models with Adversarial Gradient Integration. In *Proceedings of the Thirtieth International Joint Conference on Artificial Intelligence*, pp. 2876–2883, Montreal, Canada, August 2021. International Joint Conferences on Artificial Intelligence Organization. ISBN 978-0-9992411-9-6. doi:10.24963/ijcai.2021/396.
- Ribeiro, M. T., Singh, S., and Guestrin, C. "Why Should I Trust You?": Explaining the Predictions of Any Classifier, August 2016. URL <http://arxiv.org/abs/1602.04938>.
- Samek, W., Binder, A., Montavon, G., Bach, S., and Müller, K.-R. Evaluating the visualization of what a Deep Neural Network has learned, September 2015. URL <http://arxiv.org/abs/1509.06321>.
- Sanyal, S. and Ren, X. Discretized Integrated Gradients for Explaining Language Models. In *Proceedings of the 2021 Conference on Empirical Methods in Natural Language Processing*, pp. 10285–10299, Online and Punta Cana, Dominican Republic, 2021. Association for Computational Linguistics. doi:10.18653/v1/2021.emnlp-main.805.
- Selvaraju, R. R., Cogswell, M., Das, A., Vedantam, R., Parikh, D., and Batra, D. Grad-CAM: Visual Explanations from Deep Networks via Gradient-based Localization. *arXiv:1610.02391 [cs]*, October 2016. URL <http://arxiv.org/abs/1610.02391>.
- Shapley, L. S. *A Value for N-Person Games*. RAND Corporation, Santa Monica, 1952. doi:10.7249/P0295.
- Shrikumar, A., Greenside, P., and Kundaje, A. Learning Important Features Through Propagating Activation Differences, October 2019. URL <http://arxiv.org/abs/1704.02685>.
- Simonyan, K. and Zisserman, A. Very Deep Convolutional Networks for Large-Scale Image Recognition. *arXiv:1409.1556 [cs]*, September 2014. URL <http://arxiv.org/abs/1409.1556>.
- Simonyan, K., Vedaldi, A., and Zisserman, A. Deep Inside Convolutional Networks: Visualising Image Classification Models and Saliency Maps, April 2014. doi:10.48550/arXiv.1312.6034.
- Smilkov, D., Thorat, N., Kim, B., Viégas, F., and Wattenberg, M. SmoothGrad: Removing noise by adding noise, June 2017. URL <http://arxiv.org/abs/1706.03825>.
- Springenberg, J. T., Dosovitskiy, A., Brox, T., and Riedmiller, M. Striving for Simplicity: The All Convolutional Net. *arXiv:1412.6806 [cs]*, April 2015. URL <http://arxiv.org/abs/1412.6806>.
- Sturmfels, P., Lundberg, S., and Lee, S.-I. Visualizing the Impact of Feature Attribution Baselines. *Distill*, 5(1):10.23915/distill.00022, January 2020. ISSN 2476-0757. doi:10.23915/distill.00022.
- Sundararajan, M. and Najmi, A. The many Shapley values for model explanation, February 2020. URL <http://arxiv.org/abs/1908.08474>.
- Sundararajan, M., Taly, A., and Yan, Q. Axiomatic Attribution for Deep Networks, June 2017. URL <http://arxiv.org/abs/1703.01365>.

- Tan, H. Maximum Entropy Baseline for Integrated Gradients, April 2022. URL <http://arxiv.org/abs/2204.05948>.
- Tolhurst, D. J., Tadmor, Y., and Chao, T. Amplitude spectra of natural images. *Ophthalmic and Physiological Optics*, 12(2):229–232, 1992. ISSN 02755408, 14751313. doi:10.1111/j.1475-1313.1992.tb00296.x.
- Torralba, A. and Oliva, A. Statistics of natural image categories. *Network: Computation in Neural Systems*, 14(3): 391–412, January 2003. ISSN 0954-898X, 1361-6536. doi:10.1088/0954-898X.14.3.302.
- Tyler, C., Likova, L., Chen, C.-C., Kontsevich, L., Schira, M., and Wade, A. Extended Concepts of Occipital Retinotopy. *Current Medical Imaging Reviews*, 1(3):319–329, November 2005. ISSN 15734056. doi:10.2174/157340505774574772.
- Wandell, B. A., Brewer, A. A., and Dougherty, R. F. Visual field map clusters in human cortex. *Philosophical Transactions of the Royal Society B: Biological Sciences*, 360(1456):693–707, April 2005. ISSN 0962-8436, 1471-2970. doi:10.1098/rstb.2005.1628.
- Wandell, B. A., Dumoulin, S. O., and Brewer, A. A. Visual Field Maps in Human Cortex. *Neuron*, 56(2):366–383, October 2007. ISSN 08966273. doi:10.1016/j.neuron.2007.10.012.
- Xu, S., Venugopalan, S., and Sundararajan, M. Attribution in Scale and Space, April 2020. URL <http://arxiv.org/abs/2004.03383>.
- Yamins, D. L. and DiCarlo, J. J. Using Goal-Driven Deep Learning Models to Understand Sensory Cortex. *Nature Neuroscience*, 19(3):356–365, February 2016.
- Zeiler, M. D. and Fergus, R. Visualizing and Understanding Convolutional Networks, November 2013. URL <http://arxiv.org/abs/1311.2901>.
- Zhou, B., Khosla, A., Lapedriza, A., Oliva, A., and Torralba, A. Learning Deep Features for Discriminative Localization, December 2015. doi:10.48550/arXiv.1512.04150.
- Zintgraf, L. M., Cohen, T. S., Adel, T., and Welling, M. Visualizing Deep Neural Network Decisions: Prediction Difference Analysis, February 2017. doi:10.48550/arXiv.1702.04595.

A. Appendix

A.1. Linearity axiom of path methods

If we define a supra-model as a weighted sum of sub-models, the *linearity* axiom guarantees that the attributions of the supra-model are a weighted sum of sub-models attributions (with identical weights). For $\alpha, \beta \in \mathbb{R}$ and $f, g \in \mathcal{F}$, we have:

$$a_j(\alpha f + \beta g, \gamma, \mathbf{x}^{(i)}, \bar{\mathbf{x}}) = \alpha a_j(f, \gamma, \mathbf{x}^{(i)}, \bar{\mathbf{x}}) + \beta a_j(g, \gamma, \mathbf{x}^{(i)}, \bar{\mathbf{x}}) \quad (\text{A10})$$

A.2. Proof of IGC property: completeness to a model prediction score

Using the *completeness* axiom of IG (see Eq.3), we have:

$$\begin{aligned} \sum_{j=1}^m \mathbf{b}_j &= \sum_{j=1}^m \frac{1}{\sigma_{f(\mathbf{x})}\sigma_y} \mathbb{E}_{(\mathbf{x}, y) \sim \mathcal{D}} \left[\mathbf{a}_j^{(i)} \times (y^{(i)} - \mu_y) \right] \\ &= \frac{1}{\sigma_{f(\mathbf{x})}\sigma_y} \mathbb{E}_{(\mathbf{x}, y) \sim \mathcal{D}} \left[(y^{(i)} - \mu_y) \sum_{j=1}^m \mathbf{a}_j^{(i)} \right] \\ &= \frac{1}{\sigma_{f(\mathbf{x})}\sigma_y} \mathbb{E}_{(\mathbf{x}, y) \sim \mathcal{D}} \left[(y^{(i)} - \mu_y) (f(\mathbf{x}^{(i)}) - f(\bar{\mathbf{x}})) \right] \\ &= \frac{1}{\sigma_{f(\mathbf{x})}\sigma_y} \left(\mathbb{E}_{(\mathbf{x}, y) \sim \mathcal{D}} \left[y^{(i)} \times f(\mathbf{x}^{(i)}) \right] - \cancel{f(\bar{\mathbf{x}})\mathbb{E}_{y \sim \mathcal{D}} \left[y^{(i)} \right]} - \mu_y \mathbb{E}_{\mathbf{x} \sim \mathcal{D}} \left[f(\mathbf{x}^{(i)}) \right] + \mu_y f(\bar{\mathbf{x}}) \right) \\ &= \frac{\mathbb{E}_{(\mathbf{x}, y) \sim \mathcal{D}} \left[f(\mathbf{x}^{(i)}) \times y^{(i)} \right] - \mu_{f(\mathbf{x})}\mu_y}{\sigma_{f(\mathbf{x})}\sigma_y} \\ &= \rho(f(\mathbf{x}), y) \end{aligned} \quad (\text{A11})$$

A.3. Benchmark images

Fig.A5 shows a series of generated images used in the benchmark experiments presented in Section.4. These images are designed to respect a known property of natural images, i.e. a negative linear correspondence between log-intensities and spatial log-frequencies measured around -1.2 (Tolhurst et al., 1992). This way, while being random, these images exhibit a certain level of spatial redundancy and make the experiments feasible.

The generative procedure is as follows. We first build a 2-d gain map of the target image size filled with the spatial frequencies of the domain used by the selected Fast Fourier Transform (FFT) algorithm. We then take the norm of these cardinal frequencies and raise them to the power of -1.2. Next, resulting gain map is employed to scale complex random maps where each pixel is independently sampled from standard normal distributions for the real and imaginary parts. An inverse FFT finally generates the experimental images.

A.4. Additional benchmark propositions

In Fig.A6, we extend the work presented in Section.4 with other propositions of *dataset-wise attribution methods*. We first report two basic metrics not involving any model. Per-pixel correlation between input components \mathbf{x}_j and output y provide very blurred versions of expected patterns (Exp.A,B) or complete noise (Exp.C,D). Then, we display two-sample t-tests

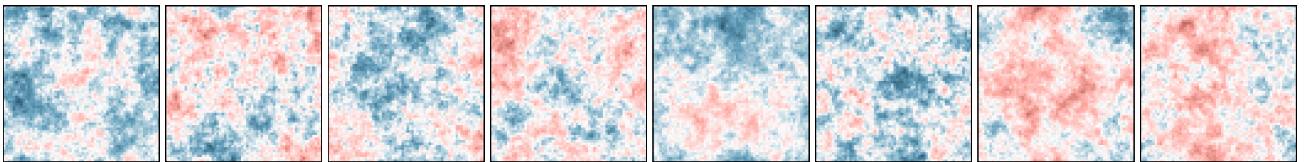


Figure A5. Samples of generated images used in the benchmark experiments presented in Section.4. Blue/red pixels indicate negative/positive values.

Integrated Gradient Correlation

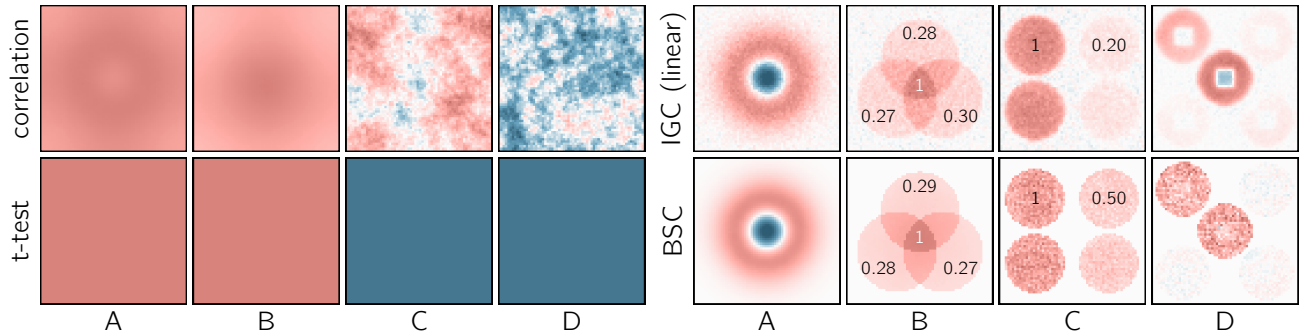


Figure A6. Benchmark of different propositions of *dataset-wise attribution methods* on four experiments labeled A-D. Attribution maps are individually scaled for a better visualization. Blue/red pixels indicate negative/positive values (except for t-tests where red pixels mean $p < 0.001$). See Section.4 for details about the experiments, and the main text for a discussion of displayed propositions.

between input components x_j corresponding to the first and the last decile of y statistics for Exp.A,B,C, and categories (one against all others) for Exp.D. Resulting maps are not interpretable because all pixels have the same attribution: all significant (Exp.A,B), i.e. it is possible to discriminate between x_j corresponding to different groups based on y ($p < 0.001$ in red); all non-significant (Exp.C,D). Together, these two results show that such simple metrics, widely used in neuroscience, do not provide selective and relevant patterns.

Secondly, we explained in Section.3 that our method inherits from IG the *implementation invariance* axiom. Here, we investigate the robustness of IGC results upon architectural changes. Unlike *IGC (model)* (see Fig.1), *IGC (linear)* (see Fig.A6) does not employ convolutional layers, but only linear layers of sizes (256, 128, 64, 32, 16). Other architectural aspects follow the logic described in Appendix.A.5. Trained multilinear models still present comparable performance with R2 scores of > 0.99 , > 0.99 , 0.78 for Exp.A,B,C, and a Top-1 accuracy of 0.76 for Exp.D. The absence of convolutional layers only makes slightly noisier attribution patterns without kernel artifacts.

Finally, we present the results of our method with Baseline Shapley as a supporting *path method* instead of Integrated Gradients. BS is slow to compute, so for practical reasons, we used only 10% of original samples. Despite a higher noise level, differences with IGC attributions are negligible.

A.5. Details of benchmark models

IGC computation details Our implementation of IGC (Lelièvre, 2025) naturally gives control over the number of IG steps and baselines. These values have been adjusted given the arbitrary rules detailed in Subsection.3.4. Final parameters are indicated in Table.A1, together with IG/IGC errors and other details. Our implementation is also designed to maximize available resources. To this end, we can adjust the batch size of output components, baselines, and inputs. Presented experiments are relatively simple, so that all output components and baselines have been processed in one batch for 10 inputs. Computation times are reported per output component. Concerning IGC attributions computed on the model, *IGC (model)*, to minimize the noise inherent to the different seeds ruling the weights' initialization and the batch collection, we trained 10 models with different seeds and finally averaged the results of the 5 best ones.

Architectural and training details We report the architecture (Table.A2) and the training details (Table.A3) of the models used in the benchmark section. By default, linear layers do not use *bias* parameters because of the use of batch normalization layers (abbreviated b.n. in tables). A *bias* is enabled only if it is stated explicitly. Reported tables summarize most of the parameters, but some additional information is required for reproducibility. First, ConvNeXt stem and block units follow the initial definition found in Liu et al. (2022). The two exceptions are the stem kernel size limited to 2, and the number of sub-block repetitions per block fixed to 3. The stochastic depth parameter is set to 0.5. Then, the weights of layers followed by Mish activation functions are initialized with normal distributions using Kaiming scaling (He et al., 2015). Otherwise, we use normal distributions with Xavier scaling (Glorot & Bengio, 2010). Furthermore, input images and output statistics are all standardized. In the case of images, this is done globally over all pixels.

A.6. Details of application models

IGC computation details Table.A4 provides similar information as in the previous section. The only difference is that computation times (and validation sizes) are reported for the subject 1 of the NSD dataset and for all output components, i.e. 2 image statistics and 2973 vertices respectively. The number of output components for the fMRI encoding model is therefore higher by several folds compared to previous applications, and IGC attributions had to be computed for a single input, a single baseline and a limited number of output components per batch. We can notice that corresponding IG error is higher than our arbitrary target of $1e-3$ (see Subsection.3.4). We could have increased the number of IG steps, but as the IGC error remains at $1e-2$, it did not worth the associated computational cost. For the fMRI decoding model, we also minimized the noise inherent to the different seeds by training 10 different models and averaging the results of the 5 best ones. However, for the fMRI encoding model, we only selected the best one because of the computation time.

Architectural and training details We report the architecture (Table.A5) and the training details (Table.A6) of the models used in the application section. Information provided in the previous section still holds for these new models. Missing details concern image and fMRI data processing. Image pixel values are rescaled in range $[0, 1]$ and linearized by inverting the default gamma associated with the sRGB format of png files. We then convert color values to luminance using the Y component of the XYZ-D65 color space and express them on a \log_2 scale. Finally, images are data augmented at training during the down sampling step. They are first resampled at double size, and then, one pixel is randomly chosen for each 2×2 local cluster. Concerning fMRI data, the standardization is applied per subject and vertex. Next, to achieve a better signal-to-noise ratio of brain activations, the NSD dataset initially provides pre-processed data that are the average of up to three presentations of the same image to the same subject. This is appropriate for the validation set, but not optimal at training. An increased data diversity usually helps models to generalize better. As a result, we used *single* fMRI data at training as a *natural* data augmentation technique. Finally, validation sets correspond to entries of image stimuli shared between subjects.

Integrated Gradient Correlation

Table A1. IGC computation details (benchmark)

	IGC				IGC (model)			
	Exp.A	Exp.B	Exp.C	Exp.D	Exp.A	Exp.B	Exp.C	Exp.D
GPU	NVIDIA RTX A2000 12GB							
validation size	100k	100k	100k	100k	10k	10k	10k	10k
IG n steps	512	512	512	512	64	64	64	64
n baselines	8	8	8	8	8	8	8	8
IG error	$< 1e-6$	$2e-4$	$9e-4$	$1e-5$	$1e-4$	$1e-4$	$1e-4$	$1e-4$
IGC error	$5e-4$	$3e-4$	$3e-3$	$2e-3$	$2e-3$	$2e-3$	$2e-3$	$2e-3$
computation time	42.2 m	1.4 h	1.4 h	1.8 h	23.9 m	24.3 m	24.4 m	26.3 m

Table A2. Model architectures (benchmark)

	Exp.A,B,C	Exp.D
input	images	images
input size	64×64	64×64
layers	ConvNeXt stem 16 ConvNeXt block 32 ConvNeXt block 64 ConvNeXt block 128 ConvNeXt block 256 flatten linear 128 + b.n. + Mish + dropout 0.25 linear 16 + b.n. + Mish + dropout 0.25 linear 1 bias	ConvNeXt stem 16 ConvNeXt block 32 ConvNeXt block 64 ConvNeXt block 128 ConvNeXt block 256 flatten linear 128 + b.n. + Mish + dropout 0.25 linear 16 + b.n. + Mish + dropout 0.25 linear 4 bias + log softmax
output	localized statistic	categories
output size	1	4

Table A3. Training details (benchmark)

	Exp.A,B,C	Exp.D
train/val. split	100k / 10k	100k / 10k
training epochs	50	100
batch size	64	64
n workers (batch)	16	8
optimizer	Adam(Kingma & Ba, 2017)	
learning rate	$5e-5$	$5e-5$
scheduler	reduce learning rate on plateau	
sched. decay	0.9	0.9
sched. patience	4	4
min learn. rate	$1e-6$	$1e-6$
loss function	MSE	NLL
computation time	53.1 m	2.0 h

Integrated Gradient Correlation

Table A4. IGC computation details (applications)

	models	
	fMRI decoding	fMRI encoding
GPU	NVIDIA RTX A2000 12GB	
validation size	1000	1000
IG n steps	64	64
n baselines	12	6
IG error	2e−5	1.5e−3
IGC error	8e−3	1e−2
computation time	1.9 m	73.7 h

Table A5. Model architectures (applications)

	fMRI decoding	fMRI encoding
input	fMRI data	images
input size	39548	64×64×3
layers	dropout 0.25 linear 128 (× 8 subjects) + b.n. + Mish (× 8 subjects) + dropout 0.25 (× 8 subjects) linear 64 + b.n. + Mish + dropout 0.25 linear 32 + b.n. + Mish + dropout 0.25 linear 16 + b.n. + Mish + dropout 0.25 linear 8 + b.n. + Mish linear 2 bias	ConvNeXt stem 32 ConvNeXt block 64 ConvNeXt block 128 ConvNeXt block 256 ConvNeXt block 512 flatten linear 256 + b.n. + Mish + dropout 0.25 linear 4321 bias (× 8 subjects)
output	image statistics	fMRI data
output size	2	4321

Table A6. Training details (applications)

	fMRI decoding	fMRI encoding
train/val. split	191882 / 7674	191882 / 7674
training epochs	75	50
batch size	8 (× 8 subjects)	4 (× 8 subjects)
n workers (batch)	1 (× 8 subjects)	2 (× 8 subjects)
optimizer	Adam(Kingma & Ba, 2017)	
learning rate	1e−4	1e−4
scheduler	reduce learning rate on plateau	
sched. decay	0.9	0.9
sched. patience	4	4
min learn. rate	1e−6	1e−6
loss function	MSE	MSE
computation time	2.4 h	7.4 h